Eur. Phys. J. D (2020) 74: 78
https://doi.org/10.1140/epjd/e2020-100606-8

THE EUROPEAN PHYSICAL JOURNAL D

Regular Article

Symmetric and antisymmetric surface plasmon polariton solitons in a metal-dielectric-metal waveguide with incoherent pumping

Zhenning Gu, Qi Liu, Yong Zhou, and Chaohua Tan[a]

School of Physics and Electronics, Shandong Normal University, 250014 Jinan, Shandong, P.R. China

Received 29 November 2019 / Received in final form 9 March 2020
Published online 22 April 2020

Abstract. We propose a scheme to realize stable linear and nonlinear propagation of symmetric and antisymmetric surface plasmon polaritons (SPPs) solitons by doping ladder-type three-level quantum emitters into the middle layer of a metal-dielectric-metal (MDM) waveguide. In linear propagation regime, we show that both symmetric and antisymmetric SPPs can acquire a gain from electromagnetically induced transparency (EIT) effect with an incoherent pumping. The EIT can be used not only to completely compensate the Ohmic loss in the metal but also to acquire a subluminal group velocity for the SPPs. We also show that in nonlinear propagation regime a huge enhancement of Kerr nonlinearity of the symmetric and antisymmetric SPPs can be obtained but with different incoherent pumping intensities. As a result, gain-assisted (1+1)-dimensional symmetric and antisymmetric subluminal surface polaritonic solitons may be produced based on the strong confinement of electric field in the MDM waveguide. Our study may have promising applications in light information processing and transmission at nanoscale level based on MDM waveguides.

1 Introduction

Surface plasmon polaritons (SPPs) are electromagnetic excitations formed by the coupling of an optical field to collective electron oscillations propagating at a metal-medium interface. The electric-field intensity of SPPs decays exponentially in the direction normal to the metal surface [1]. On the nanoscale, SPPs can overcome the diffraction limit, giving them a strong potential to guide and manipulate light [2]. Thus, SPPs have many potential applications, such as all-optical logic gates [3], super-resolution imaging [4], photovoltaic power generation [5,6], biosensors [7,8], nanomaterials [9], and lithography [10].

Recently, the coherent control of SPPs strongly interacting with systems with multiple energy levels has attracted significant interest, especially for the study of quantum interference and the nonlinear properties of SPPs. Quantum interference can be used to regulate the optical properties of a medium, which produces a series of important optical phenomena, such as electromagnetically induced transparency (EIT) [11–14], active Raman gain [15–17], coherent population trapping [18], and so on. By exploiting these effects, linear and nonlinear propagation of SPPs has been realized, such as polariton frequency combs and breather propagation [19], surface-polariton rogue waves [12], and solitons [20], the latter of which have become of paramount importance due to their potential applications to SPPs soliton storage [21], compact photonic chips [19], all-optical communication [22], and more.

When the size of conventional optical circuits is reduced to the nanometer scale, the propagation of light becomes limited by diffraction. However, SPPs offer an avenue for constructing such nanoscale photonics and devices [23]. Plasmonic waveguides can confine and manipulate SPPs on the nanoscale and support the propagation of SPPs at their metal-dielectric interface. They can thus be used to guide light into subwavelength structures beyond the diffraction limitation [24]. Therefore, plasmonic waveguides are considered to be an ideal optical instrument to control propagating SPPs [25,26].

To date, various plasmonic waveguides have been studied, such as planar waveguides [27], single-layer waveguides [28], multi-layer waveguides, cylindrical waveguides [13], and slot waveguides [29]. A popular waveguide is the multi-layer waveguide, such as the dielectric-metal-dielectric waveguide [30,31] or the metal-dielectric-metal (MDM) waveguide [25,26,32]. It is found such multi-layer structures generate a huge nonlinearity and support a surface polaritons solitons [33–37], and even can control the interaction of the solitons [38]. MDM waveguides are considered to be the most promising candidates for manipulation and transmission of light [39] because they have the advantages that they are easy to manufacture, offer deep-subwavelength confinement of light, and have relatively long propagation distances [25,40].

Although MDM waveguides have many advantages, they inevitably suffer from Ohmic loss at optical frequencies

[a] e-mail: tanch@sdnu.edu.cn

because they are enclosed in metal [14,41], which reduces the propagation distance of SPPs. To overcome Ohmic losses in this work, we introduce an incoherent pumping which produces a modulatable mechanism [42] that provides the system with active gain and can change the linear and nonlinear response of the system. Two types of propagation modes (symmetric mode and antisymmetric mode) are possible when SPPs propagate in MDM waveguides [43–45]. The results of this research show that, in the linear propagation regime, both symmetric and antisymmetric SPPs can extract gain from the waveguide under EIT generated by incoherent pumping. EIT can be used not only to completely compensate for Ohmic losses in the metal but also to endow the SPPs with a subluminal group velocity. In the nonlinear propagation regime, the Kerr nonlinearity is strongly enhanced by the EIT effect together with the confinement of the MDM waveguide. Consequently, gain-assisted (1+1)-dimensional symmetric and antisymmetric subluminal surface plasmon polariton solitons may be produced in the MDM waveguide, and propagate to a long distance (up to several centimeters for symmetric mode, and several millimeters for antisymmetric mode). The results predicted by this work may have applications in the study of light transmission at the nanoscale.

This paper is arranged as follows: Section 2 introduces the theoretical model used to describe SPPs, Section 3 discusses the linear propagation characteristics of the two modes, and Section 4 investigates the nonlinear characteristics of the two modes and derives the nonlinear Schrödinger equation (NLSE). At the same time, the possibility of forming solitons in the two modes is discussed, and the propagation of solitons is numerically simulated. Finally, Section 5 summarizes the article.

2 Model

Figure 1 shows the theoretical model we study in this work. The system consists of a three-layer waveguide structure composed of a central dielectric layer sandwiched between two metal layers, i.e., MDM waveguide. The thickness of the dielectric layer is d. The central dielectric layer fills the space ($|x| < d/2$), and its permittivity and permeability are ε_1 and μ_1, respectively. The upper and lower layers are metal, and can be treated as extending infinitely to both sides of the dielectric layer, ($|x| \geq d/2$). The permittivity and permeability of the metal are $\varepsilon_2(\omega)$ and $\mu_2(\omega)$, respectively.

Such a MDM waveguide can support both transverse electric (TE) and transverse magnetic (TM) modes. However, TE SPPs are known to be ineffective in this system [46], thus we consider only the TM mode. We assume that the SPPs propagate in the positive x direction.

The TM modes we consider here have a specific symmetry of the magnetic field intensity $\mathbf{H}$. Note that when we discuss symmetry in this paper, we are referring the symmetry of magnetic field profile with respect to the center plain of the dielectric layer in MDM configuration. We solve the Maxwell equations for the TM mode and obtain the following expressions for the electric field of the two propagation modes (the detail discussion about Maxwell equations and boundary conditions are given in Appendix A):

Electric field for symmetric propagation mode:

$$\mathbf{E}(\mathbf{r},t) = \begin{cases} (k\mathbf{e}_z - ik_{x2}\mathbf{e}_x)\frac{\varepsilon_1}{k\varepsilon_2}\cosh(k_{x1}\frac{d}{2})e^{-k_{x2}(x-\frac{d}{2})+i(kz-\omega_q t)}, & x > \frac{d}{2} \\ \left[\cosh(k_{x1}x)\mathbf{e}_z + \frac{ik_{x1}}{k}\sinh(k_{x1}x)\mathbf{e}_x\right]e^{i(kz-\omega_q t)}, & -\frac{d}{2} < x < \frac{d}{2} \\ (k\mathbf{e}_z + ik_{x2}\mathbf{e}_x)\frac{\varepsilon_1}{k\varepsilon_2}\cosh(k_{x1}\frac{d}{2})e^{k_{x2}(x+\frac{d}{2})+i(kz-\omega_q t)}, & x < -\frac{d}{2}. \end{cases} \quad (1)$$

Electric field for antisymmetric propagation mode:

$$\mathbf{E}(\mathbf{r},t) = \begin{cases} (k\mathbf{e}_z - ik_{x2}\mathbf{e}_x)\frac{\varepsilon_1}{k\varepsilon_2}\sinh(k_{x1}\frac{d}{2})e^{-k_{x2}(x-\frac{d}{2})+i(kz-\omega_q t)}, & x > \frac{d}{2} \\ \left[\sinh(k_{x1}x)\mathbf{e}_z + \frac{ik_{x1}}{k}\cosh(k_{x1}x)\mathbf{e}_x\right]e^{i(kz-\omega_q t)}, & -\frac{d}{2} < x < \frac{d}{2} \\ -(k\mathbf{e}_z + ik_{x2}\mathbf{e}_x)\frac{\varepsilon_1}{k\varepsilon_2}\sinh(k_{x1}\frac{d}{2})e^{k_{x2}(x+\frac{d}{2})+i(kz-\omega_q t)}, & x < -\frac{d}{2}. \end{cases} \quad (2)$$

In equations (1) and (2), $\mathbf{e}_l (l = x, y, z)$ is a unit vector along the l direction, and the wave number $k_{xl}^2 = k^2 - (\omega_q/c)^2\varepsilon_l$, where $l = 1$ corresponds to the dielectric and $l = 2$ corresponds to the metal. The propagation constants of the SPPs and their dispersion relation are obtained by using the boundary conditions. The dispersion relationship for the symmetric mode satisfies $\varepsilon_1 k_{x2} + \varepsilon_2 k_{x1}\tanh(k_{x1}\frac{d}{2}) = 0$, and the dispersion relationship for the antisymmetric mode satisfies $\varepsilon_1 k_{x2} + \varepsilon_2 k_{x1}\coth(k_{x1}\frac{d}{2}) = 0$.

The ladder-type quantum emitter dopes the intermediate dielectric layer, which is typically composed of atoms, quantum dots, rare-earth ions, semiconductor quantum wells, etc. The ladder-type quantum emitter couples the weak probe field to the strong control field. Figure 1b shows a diagram of the energy-level structure and excitation configuration of the ladder-type quantum emitter. The upper state $|3\rangle$ is an excited state, and the state $|3\rangle$ ($|2\rangle$) is considered to decay spontaneously to state $|2\rangle$ ($|1\rangle$) with decay rate Γ_{23} (Γ_{12}). The angular frequency and the half Rabi frequency of the weak probe field are ω_p and Ω_p, respectively, and the weak probe field couples states $|2\rangle$ to $|1\rangle$. The angular frequency and the half Rabi frequency of the strong control field are ω_c and Ω_c, respectively, and the strong probe field couples states $|3\rangle$ to $|2\rangle$. In order to realize lossless SPPs, we introduce an incoherent pumping in this system to provide active gain [47], driving the $|1\rangle \rightarrow |3\rangle$ transition at the rate Γ_{31}.

The main purpose of this work is to study the resonant coupling of symmetric and antisymmetric TM SPPs in MDM waveguide with quantum emitters doped into the dielectric layer. The interaction occurs only in the dielectric, thus we can express the electric field as

$$\mathbf{E}(\mathbf{r},t) = \sum_{q=p,c} \mathcal{E}_q(z,t)\mathbf{u}_\mathbf{q}(z)e^{i(k_q z-\omega_q t)} + \text{c.c.}, \quad (3)$$

where $\mathbf{u}_\mathbf{q}(x) = \cosh(k_{x1}x)\mathbf{e}_z + (ik_{x1}/k)\sinh(k_{x1}x)\mathbf{e}_x$ (for symmetric TM mode) or $\mathbf{u}_\mathbf{q}(x) = \sinh(k_{x1}x)\mathbf{e}_z + (ik_{x1}/k)\cosh(k_{x1}x)\mathbf{e}_x$ (for antisymmetric TM mode) is

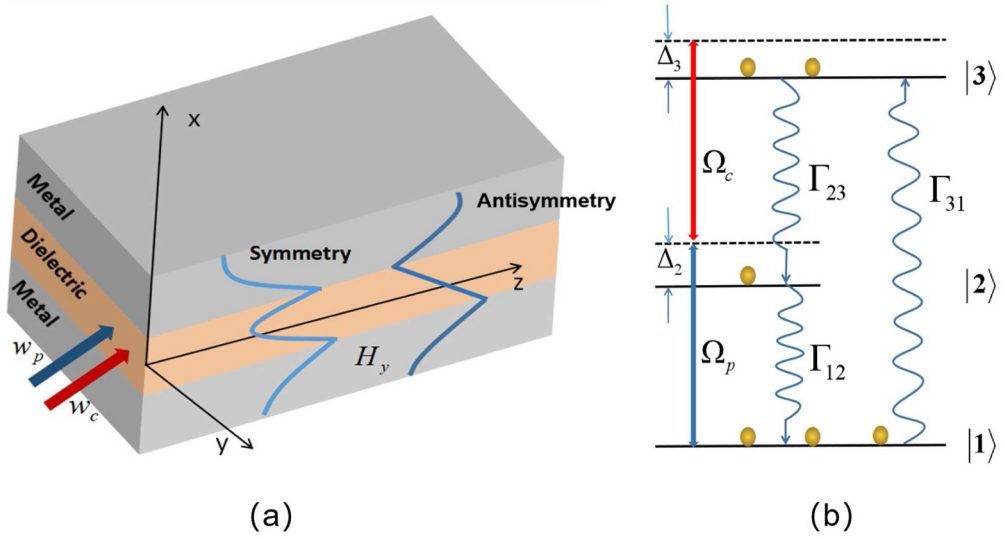

Fig. 1. Excitation and propagation of SPPs in MDM structures. (a) MDM three-layer waveguide structure. The two curves represent the H_y field of SPPs for the symmetric and antisymmetric modes, respectively, and all fields propagate along the positive z axis. (b) Diagram showing the energy levels and excitation configuration of a ladder-type quantum emitter. The state $|3\rangle$ ($|2\rangle$) is considered to decay spontaneously to state $|2\rangle$ ($|1\rangle$) with decay constant Γ_{23} (Γ_{12}), the transition $|3\rangle \rightarrow |1\rangle$ is forbidden, Γ_{31} corresponds to incoherent pumping, and Δ_2 and Δ_3 are the single- and two-photon detunings, respectively.

the constraint function of SPPs in the z direction, $\mathcal{E}_p$ and $\mathcal{E}_c$ are envelope functions of the probe field and control field, respectively, k_p and k_c are the wave numbers before the probe field or control field enters the dielectric, respectively, and ω_p and ω_c are the center frequencies of the probe and control fields, respectively. In the following, as in references [36,37], for simplicity we take the linear mode function for the electric field[1] when the nonlinear effect occurs in the system[2].

Under the electric-dipole approximation and the slowly varying envelope approximation, the Hamiltonian of the system in the interaction picture is

$$\hat{H}_{\text{int}} = -\hbar\sum_{j=1}^{3}\Delta_j|j\rangle\langle j| - \hbar[\zeta_p(x)e^{i\theta_p}\Omega_p|2\rangle\langle 1| + \zeta_c(x)e^{i\theta_c}\Omega_c|3\rangle\langle 2| + \text{h.c.}], \tag{4}$$

where $\Delta_2 = \omega_p - (\omega_2 - \omega_1)$ and $\Delta_3 = \omega_p + \omega_c - (\omega_3 - \omega_1)$ are the single- and two-photon detunings of the optical field. The eigenfrequency of energy level l is ω_l ($l = 1, 2, 3$). In equation (4), we define the half Rabi frequency as $\Omega_{jk} = \mathcal{E}_{jk}|\mathbf{p_{jk}}|/\hbar$, where $\Omega_p = \mathcal{E}_{21}|\mathbf{p_{21}}|/\hbar$ and $\Omega_c = \mathcal{E}_{32}|\mathbf{p_{32}}|/\hbar$ are the half Rabi frequency of the probe field and control field, respectively, $\mathcal{E}_{jk}$ is the amplitude of the corresponding optical field, $\mathbf{p_{jk}}$ is the electric-dipole matrix element representing the energy-level transition from $|j\rangle$ to $|k\rangle$ along the $\mathbf{e_{jk}}$ direction. $\zeta_c(x) = \mathbf{e_{23}} \cdot \mathbf{u_c}(x), \zeta_p(x) = \mathbf{e_{12}} \cdot \mathbf{u_p}(x)$, and the mode function $\zeta_{p,c}(x)$ is a rapidly varying function with respect to x.

The Bloch equations describing the dynamic evolution of this system are expressed as

$$\begin{aligned}
&i\left(\frac{\partial}{\partial t} + \Gamma_{31}\right)\sigma_{11} - i\Gamma_{12}\sigma_{22} + \zeta_p^*(x)\Omega_p^*\sigma_{21}e^{-i\theta_p^*} - \zeta_p(x)\Omega_p\sigma_{21}^*e^{i\theta_p} = 0,\\
&i\left(\frac{\partial}{\partial t} + \Gamma_{12}\right)\sigma_{22} - i\Gamma_{23}\sigma_{33} + \zeta_p(x)\Omega_p\sigma_{21}^*e^{i\theta_p} + \zeta_c^*(x)\Omega_c^*\sigma_{32}e^{-i\theta_c^*} - \zeta_p^*(x)\Omega_p^*\sigma_{21}^*e^{-i\theta_p^*} - \zeta_c(x)\Omega_c\sigma_{32}^*e^{i\theta_c} = 0,\\
&i\left(\frac{\partial}{\partial t} + \Gamma_{23}\right)\sigma_{33} - i\Gamma_{31}\sigma_{11} + \zeta_c(x)\Omega_c\sigma_{32}^*e^{i\theta_c} - \zeta_c^*(x)\Omega_c^*\sigma_{32}^*e^{-i\theta_c^*} = 0,\\
&\left(i\frac{\partial}{\partial t} + d_{21}\right)\sigma_{21} + \zeta_c^*(x)\Omega_c^*\sigma_{31}e^{-i\theta_c^*} + \zeta_p(x)\Omega_p e^{i\theta_p}(\sigma_{11} - \sigma_{22}) = 0,\\
&\left(i\frac{\partial}{\partial t} + d_{31}\right)\sigma_{31} - \zeta_p(x)\Omega_p\sigma_{32}e^{i\theta_p} + \zeta_c(x)\Omega_c\sigma_{21}e^{i\theta_c} = 0,\\
&\left(i\frac{\partial}{\partial t} + d_{32}\right)\sigma_{32} - \zeta_p^*(x)\Omega_p^*\sigma_{31}e^{-i\theta_p^*} + \zeta_c(x)\Omega_c e^{i\theta_c}(\sigma_{22} - \sigma_{33}) = 0,
\end{aligned} \tag{5}$$

[1] Such approach is similar to the averaging method used in references [36,37]. A more rigorous approach should account for nonlinear terms in boundary conditions and nontransverse character of the electric field. In this way, the mode function in high-order approximations will be a little different. However, as shown by Marini and Skryabin [49], the difference between the two approaches is not significant if the wavelength of the excitation is not too short.

[2] Because both the probe and control fields used are weak and far from material resonances, both the dielectric and the metal can be safely taken as linear optical materials. The nonlinear optical effect in our system comes from the resonance between the quantum emitters and the probe and control fields.

where $d_{21} = \Delta_2 + i\gamma_{21}$, $d_{31} = \Delta_3 + i\gamma_{31}$, and $d_{32} = \Delta_3 - \Delta_2 + i\gamma_{32}$, $\gamma_{jl} = (\Gamma_j + \Gamma_l)/2$ and $\theta_{p,c} = (k_{p,c} + k_{2,3} - k_{1,2}) \cdot z$ the phase mismatch caused by the eigen dispersion of SPPs.

The propagation of the electric field in the system satisfies the classical Maxwell equation $\nabla^2\mathbf{E} - (1/c^2)(\partial^2\mathbf{E}/\partial t^2) = (1/\epsilon_0 c^2)(\partial^2\mathbf{P}/\partial t^2)$, and the system's polarization is given by $\mathbf{P}(\mathbf{r},t) = N_a \mathbf{p_{lj}} \sigma_{jl} e^{i[(k_j - k_i)z - [(\omega_j - \omega_k) + (\Delta_j - \Delta_k)]t]} + \text{c.c.}$, where N_a is the number density of quantum emitter dopants (the doped layer is in the range $|z| < d/2$). Under the slowly varying envelope approximation, the Maxwell equation can be written as

$$i\left(\frac{\partial}{\partial z} + \frac{1}{c}\frac{n_1^2}{n_{\text{eff}}}\frac{\partial}{\partial t}\right)\Omega_p e^{i\theta_p} + \kappa_{12}\langle\sigma_{21}\rangle = 0, \tag{6}$$

where $\kappa_{12} = N_a\omega_q|\mathbf{p_{12}}|^2/2\hbar\varepsilon_0 c n_{\text{eff}}$ is the coupling constant of the interaction between the SPPs and the quantum emitters, and $n_{\text{eff}} \equiv ck_{21}/\omega_{21}$ is the effective refractive index. To derive equation (6), we ignore the evolution of the control field, the diffraction of probe field in y direction, and define the spatial averaging as $\langle\Psi(x)\rangle \equiv \int_{-\infty}^{+\infty} dx\zeta_p^*(x)\Psi(x)/\int_{-\infty}^{+\infty} dx|\zeta_p(x)|^2$, where Ψ is an arbitrary function.

3 Linear properties of SPPs

3.1 Base state

We first study the linear excitation of SPPs in symmetric and antisymmetric modes, thus we need to know the base state of the system (i.e., the state with no input probe field, only the control field irradiates the system to prepare the dressed state). In this state $\Omega_p = 0$. We solve the Maxwell–Bloch(MB) equations (5) and (6) by using the multiscale method [48] and making use of asymptotic expansions $\sigma_{ij} = \sum_q \epsilon^q \sigma_{ij}^{(q)}$ $(q = 0, 1, 2, 3)$, and $\Omega_p = \sum_q \epsilon^q \Omega^{(q)}$ $(q = 1, 2, 3)$, where ϵ is a small dimensionless physical parameter and the various quantities on the right-hand side of the equal sign are functions of multiscale variables $z_q = \epsilon^q z$ $(q = 0, 1, 2)$, and $t_q = \epsilon^q t$ $(q = 0, 1)$. We get the initial steady-state of the system, i.e., the zeroth-order solution of the MB equations

See equations (7a)−(7d) next page.

and $\sigma_{21}^{(0)} = \sigma_{31}^{(0)} = 0$. With no incoherent pumping (i.e., $\Gamma_{31} = 0$), the system adheres to conservation of particle number, $\sum_{j=1}^{3}\sigma_{jj} = 1$, and the initial state of the system reduces to $\sigma_{11}^{(0)} = 1, \sigma_{22}^{(0)} = \sigma_{33}^{(0)} = \sigma_{32}^{(0)} = \sigma_{21}^{(0)} = \sigma_{31}^{(0)} = 0$. This indicates that, when only the control field is present, the particles only populate on the ground state $|1\rangle$. With the addition of incoherent pumping, $\sigma_{22}^{(0)} \neq 0$, which means that the particles are pumped to the $|2\rangle$ state, and the system can provide gain for the probe field, thereby suppressing the absorption of the probe field.

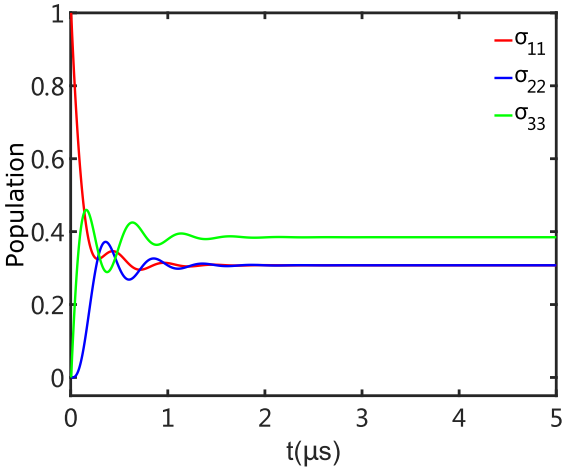

Fig. 2. Time evolution of population on each states.

We also study how the state population evolves over time. As shown in Figure 2, the red, blue, and green lines represent σ_{11}, σ_{22}, and σ_{33}, respectively. The population of each energy level stabilizes after a few microseconds, and σ_{22} does not disappear, which means that the system provides gain for the probe field. The numerical calculation uses the following physical parameters: $\Gamma_{12} = \Gamma = 6 \times 10^6\,\text{s}^{-1}$, $\Gamma_{23} = 1 \times 10^3\,\text{s}^{-1}$, $\Omega_c = \Gamma$ [47], $\kappa_{12} = 1 \times 10^{10}\,\text{cm}^{-1}\,\text{s}^{-1}$, the incoherent pumping $\Gamma_{31} = 0.5\Gamma$, the wavelength is 780 nm, the dielectric thickness $d = 200\,\text{nm}$, $\varepsilon_1 = 4$, $\mu_1 = 1$, $\varepsilon_2 = -29.25 + 0.57i$, $\mu_2 = 1$ (selected from metallic silver at $\lambda = 780\,\text{nm}$), $|\mathbf{p}_{12}| = 2.6 \times 10^{-30}\,\text{C} \cdot \text{cm}$.

3.2 Linear dispersion relation of SPPs

Continuing our solution of the MB equations with the multiscale method, we can get the first-order solution:

$$\Omega_p^{(1)} = Fe^{i\theta}, \tag{8a}$$

$$\sigma_{21}^{(1)} = \frac{D_1}{D}\zeta_p(x)\Omega_p^{(1)}e^{i\theta_p}, \tag{8b}$$

$$\sigma_{31}^{(1)} = \frac{D_2}{D}\zeta_p(x)\Omega_p^{(1)}e^{i\theta_p}, \tag{8c}$$

with $\theta = K(\omega)x_0 - \omega t_0$, $D = (\omega + d_{21})(\omega + d_{31}) - |\zeta_c(x)\Omega_c e^{i\theta_c}|^2$, $D_1 = (\omega + d_{31})(\sigma_{22}^{(0)} - \sigma_{11}^{(0)}) - \zeta_c^*(x)\Omega_c^*\sigma_{32}^{(0)}e^{-i\theta_c^*}$, $D_2 = (\omega + d_{21})\sigma_{32}^{(0)} - (\sigma_{22}^{(0)} - \sigma_{11}^{(0)})\zeta_c(x)\Omega_c e^{i\theta_c}$, where ω is the frequency deviation with respect to the center frequency ω_p, and F is the evolution function of the slow variables z_1, z_2, and t_1, and $K(\omega)$ is the linear dispersion relation for the SPPs:

$$K(\omega) = \frac{\omega}{c}\frac{n_1^2}{n_{\text{eff}}} + \kappa_{12}\left\langle\frac{D_1}{D}\zeta_p(x)\right\rangle. \tag{9}$$

The real part of the linear dispersion relation $K(\omega)$ characterizes the dispersion, and the imaginary part of the linear dispersion relation $K(\omega)$ characterizes the linear absorption generally.

$$\sigma_{11}^{(0)} = \frac{i\Gamma_{12}\Gamma_{23}|d_{32}|^2 + |\zeta_c(x)\Omega_c e^{i\theta_c}|^2(d_{32}-d_{32}^*)\Gamma_{12}}{i(\Gamma_{12}\Gamma_{23}+\Gamma_{23}\Gamma_{31}+\Gamma_{12}\Gamma_{31})|d_{32}|^2 + |\zeta_c(x)\Omega_c e^{i\theta_c}|^2(d_{32}-d_{32}^*)(\Gamma_{12}+2\Gamma_{31})}, \tag{7a}$$

$$\sigma_{22}^{(0)} = \frac{\Gamma_{31}}{\Gamma_{12}}\sigma_{11}^{(0)}, \tag{7b}$$

$$\sigma_{33}^{(0)} = 1 - (\sigma_{11}^{(0)} + \sigma_{22}^{(0)}), \tag{7c}$$

$$\sigma_{32}^{(0)} = \frac{\zeta_c(x)\Omega_c}{d_{32}}(\sigma_{33}^{(0)} - \sigma_{22}^{(0)})e^{i\theta_c}, \tag{7d}$$

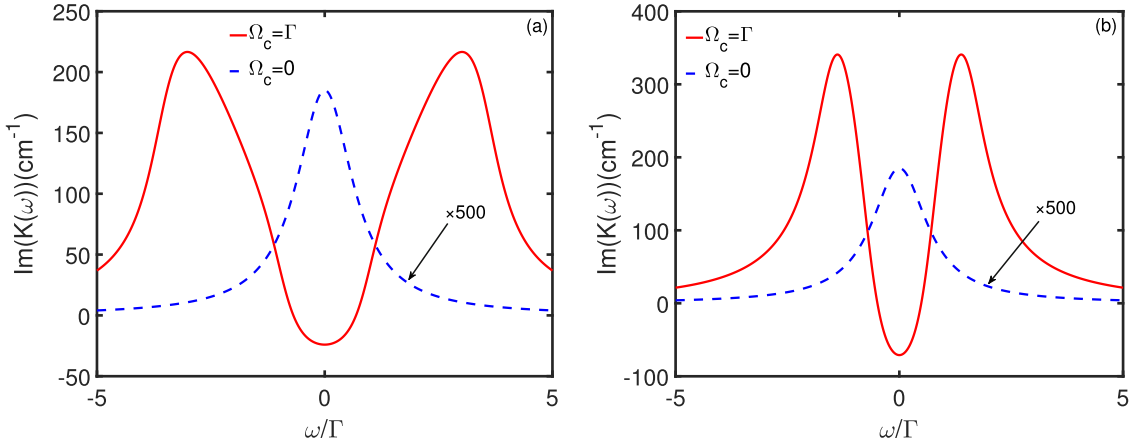

Fig. 3. The linear absorption $\mathrm{Im}(K)$ as function of the frequency ω/Γ for (a) the symmetric mode and (b) the antisymmetric mode. The blue dashed line shows the absorption of the system with $\Omega_c = 0$, and the red solid line shows the absorption of the system with $\Omega_c = \Gamma$. The values for the blue dashed lines are multiplied by 500.

Figures 3a and 3b shows the linear absorption $\mathrm{Im}(K)$ as function of the frequency ω/Γ in the symmetric (antisymmetric) mode. The blue dashed line shows the absorption of the system with $\Omega_c = 0$, and the red solid line shows the absorption of the system with $\Omega_c = \Gamma$. The results indicate that, with no control field, the absorption of the probe field peaks at the center frequency ($\omega = 0$) is large, which means that the probe field is strongly absorbed.

To facilitate observation and comparison, the absorption curves when the control field is zero are multiplied by 500. With the control field present, the absorption peak of the probe field changes to an absorption dip at the center frequency, which means that the absorption of the probe field is strongly suppressed; in other words, a transparent window is created. In addition, incoherent pumping allows the probe field to extract gain from the system. Note that $\mathrm{Im}(K) < 0$, which corresponds to gain. In addition, the transparent window in the symmetric mode is wider than in the antisymmetric mode, which indicates that EIT is stronger for the symmetric mode.

The gain of the system depends on Γ_{31}. To select the appropriate incoherent pumping, we study the relationship between the incoherent pumping Γ_{31}/Γ and the gain $-\mathrm{Im}(K)|_{\omega=0}$. The red (blue) line in Figure 4a shows the relationship between Γ_{31}/Γ and $-\mathrm{Im}(K)|_{\omega=0}$ in the symmetric (antisymmetric) mode. Upon increasing Γ_{31}/Γ, $-\mathrm{Im}(K)|_{\omega=0}$ in the symmetric mode increases, indicating that the system gain increases. In the antisymmetric mode, $-\mathrm{Im}(K)|_{\omega=0}$ increases initially, and then levels off, indicating that the gain saturates.

Figure 4b shows the group velocity $\tilde{V}_g = [\partial \mathrm{Re}(K)/\partial\omega]^{-1}$ as a function of the frequency ω/Γ. The results show that one implements fast light and the other implements slow light. But with different parameters, the group velocity for both symmetric and antisymmetric mode could be $\tilde{V}_g > 0$, which leads to slow light in the system. The physical reason explaining the appearance of the subluminal propagation speed is that the system is saturated. The system parameters are the same as those used before.

4 Symmetric and antisymmetric SPPs solitons

We next discuss nonlinear surface-polarization activation in the symmetric and antisymmetric modes of this system. We first need to obtain a nonlinear envelope function to control the evolution of the probe light. We use the multiscale method to solve the MB equations and retain the second-order solutions of σ_{jj} and σ_{ij} (see appendix for detailed expressions). To prevent the divergence of the solution of $\Omega_p^{(2)}$, the following condition must be satisfied:

$$i\left(\frac{\partial F}{\partial z_1} + \frac{1}{V_g}\frac{\partial F}{\partial t_1}\right) = 0. \tag{10}$$

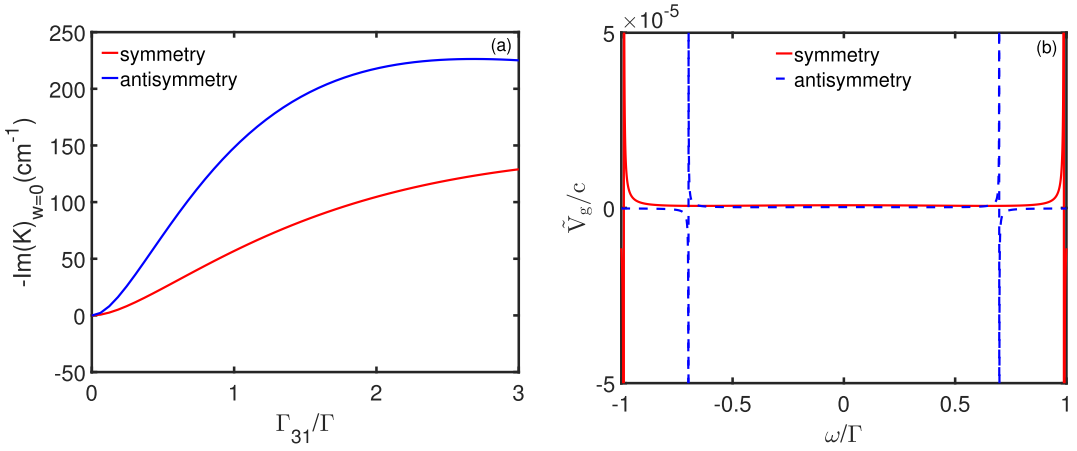

Fig. 4. (a) The gain $-\mathrm{Im}(K)|_{\omega=0}$ as a function of Γ_{31}/Γ at the center frequency. The red (blue) line shows the symmetric (antisymmetric) mode. (b) $\tilde{V}_g/c$ as a function of the frequency ω with $\Omega_c = \Gamma$. The red solid line shows the symmetric mode, and the blue dashed line shows the antisymmetric mode.

The propagation equation (10) is satisfied by the envelope function F of the probe field. In equation (10), the group velocity is

$$V_g = \left[\frac{1}{c}\frac{n_1^2}{n_{\mathrm{eff}}} + \kappa_{12}\frac{D_2\zeta_c^*\Omega_c^* e^{-i\theta_c^*} - (\omega + d_{31})D_1}{D^2}\right]^{-1}. \tag{11}$$

For the solution of $\Omega_p^{(3)}$ to converge, the following condition must be satisfied:

$$i\frac{\partial}{\partial z_2}F - \frac{1}{2}\frac{\partial^2 K(\omega)}{\partial\omega^2}\frac{\partial^2 F}{\partial t_1^2} - W|F|^2 F e^{-2\bar{\alpha}z_2} = 0. \tag{12}$$

Equation (12) is a nonlinear propagation equation for the third-order probe optical envelope function F, where $\bar{\alpha} = \alpha/\epsilon^2$ and $\alpha = \mathrm{Im}(K + k)$. The nonlinear coefficient W describing the probe-field self-phase modulation is given by

$$W = \kappa_{12}\left\langle \frac{(\omega + d_{31})(a_{11}^{(2)} - a_{22}^{(2)}) + \zeta_c^*(x)\Omega_c^* e^{-i\theta_c^*}a_{32}^{(2)}}{D} \times \zeta_p(x)|\zeta_p(x)e^{i\theta_p}|^2\right\rangle. \tag{13}$$

The third-order (Kerr) nonlinear polarizability is proportional to the self-phase modulation nonlinear coefficient, and the relationship is as follows:

$$\chi_{pp}^{(3)} = \frac{2c}{\omega_p}\frac{|\mathbf{p}_{12}|^2}{\hbar^2}W. \tag{14}$$

Figure 5 shows the third-order nonlinearity as functions of the frequency ω for both symmetric and antisymmetric SPPs. The red solid (blue dashed) line shows the real (imaginary) part of $\chi_{pp}^{(3)}$. The results show that the system is pumped incoherently (we choose incoherent pumping with $\Gamma_{31} = 0.17\,\Gamma$). We can find that the Kerr effect in the system is very large. And also, in the symmetric and antisymmetric modes, when $\Delta_2 < 0$, the real part is much greater than the imaginary part, which plays a crucial role in the formation and stable propagation of SPPs solitons in the system. Here, in order to facilitate observation and comparison, the imaginary part are multiplied by 10 and 5, respectively.

Simultaneous equations (10) and (12) give the following nonlinear envelope equation describing the nonlinear propagation of the probe light in the waveguide:

$$i\left(\frac{\partial}{\partial z} + \alpha\right)U - \frac{K_2}{2}\frac{\partial^2}{\partial\tau^2}U - W|U|^2U = 0, \tag{15}$$

where $\tau = t - z/V_g$, $U = \epsilon F\exp(-i\alpha z)$, and $K_2 \equiv \partial^2 K(\omega)/\partial\omega^2$ is the group velocity dispersion, which is given by

$$K_2 = 2i\kappa_{12}\left\langle \frac{(\omega + d_{31})a_{21}^{(2)}\zeta_c(x) - \Omega_c^* a_{31}^{(2)}|\zeta_c(x)|^2 e^{-i\theta_c^*}}{D}\right\rangle, \tag{16}$$

where the coefficients $a_{21}^{(2)}$ and $a_{31}^{(2)}$ are given in Appendix B. Note that we have omitted the higher-order dispersion in equation (15). This approximation is valid when the pulse duration is large enough such that the higher-order dispersion do not take significant effect [50,51].

The coefficients of the equation (15) are all complex, i.e., it is a Ginzberg–Landau equation, and the complex-coefficient equation is usually nonintegrable, which does not allow stable soliton solution in general. In general, the formation and propagation of surface polaritons in an optical system are possible if two conditions are satisfied: (1) the absorption of the probe light in the system must be sufficiently small, and (2) the dispersion and nonlinear effect of light in the system must be balanced. Therefore, if the real part of the coefficient of the equation (15) is much greater than the imaginary part, the soliton solution will be very stable and the soliton can propagate a long distance with the waveform unchanged. Fortunately, we can find a reasonable set of physical parameters under the

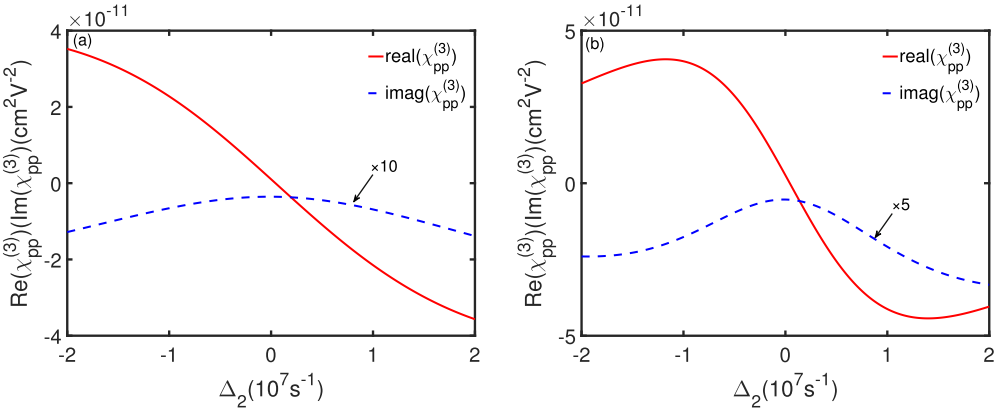

Fig. 5. The third-order nonlinearity for (a) symmetric mode and (b) antisymmetric mode. The red solid (blue dashed) line shows the real (imaginary) part of $\chi_{pp}^{(3)}$. The values of the blue dashed lines in panel (a) and (b) are multiplied by 10 and 5, respectively.

EIT condition, so the real part of the coefficients in the equation (15) are much greater than the imaginary parts.

Ignoring the imaginary parts, and choosing $\omega = 0$, we can obtain the dimensionless form of the above formula, which gives

$$i\frac{\partial u}{\partial s} + \frac{\partial^2 u}{\partial \sigma^2} + 2|u|^2 u - \frac{2\tau_0^2 u}{\tilde{K}_2}\alpha = 0, \tag{17}$$

where $s = -z/2L_D$, $\sigma = \tau/\tau_0$, $u = U/U_0$, τ_0 is the duration of the pulse (which can be called the pulse width), $L_D = \tau_0^2/\tilde{K}_2$ is the characteristic dispersion length of the system, $U_0 = (1/\tau_0)\sqrt{\tilde{K}_2/\tilde{W}}$ is the characteristic half Rabi frequency of the system, and $\tilde{K}_2$ and $\tilde{W}$ are the real parts of K_2 and W, respectively.

We will show later that we can choose a set of physical system parameters to make $\alpha \approx 0$, thus we ignore it in later analyze. In fact, when propagation length is far less than the absorption length (as the case we discussed), ignoring the absorption is a well approximation [41,46]. This leads to a standard nonlinear Schrödinger equation (NLSE), which is fully integrable:

$$i\frac{\partial u}{\partial s} + \frac{\partial^2 u}{\partial \sigma^2} + 2|u|^2 u = 0. \tag{18}$$

We get various soliton solutions from this dimensionless NLSE. The single-soliton solution can be simplified to the form $u = sech(\sigma)\exp(is)$, which can be expressed with the half Rabi frequency as follows:

$$\Omega_p(z,t) = \frac{1}{\tau_0}\sqrt{\frac{\tilde{K}_2}{\tilde{W}}}sech\left[\frac{1}{\tau_0}(\tau - \frac{z}{\tilde{V}_g})\right]\exp\left[i\tilde{K}_0 x + i\frac{z}{2L_D}\right]. \tag{19}$$

This equation describes a bright soliton, where $\tilde{K}_0 = \mathrm{Re}(K)|_{\omega=0}$, and $\tilde{V}_g = \mathrm{Re}(\partial K/\partial\omega)|_{\omega=0}$ is the group velocity at which a bright SPPs soliton propagates.

We now present the physical parameters required for the formation and propagation of a set of symmetric and antisymmetric SPPs. For symmetric SPPs, we use $\Gamma_{31} = 0.17\,\Gamma$, $\Delta_2 = 2.07\,\Gamma$, $\Delta_3 = -0.4\,\Gamma$, and $\tau_0 = 6\times10^{-7}\,\mathrm{s}$, and we calculate $\mathrm{Im}(K+k) = -0.01\,\mathrm{cm}^{-1}$. In addition, we get $L_D = 3.59\,\mathrm{cm}, K_2 = (8.34+1.69)\times10^{-14}\,\mathrm{cm}^{-1}\,\mathrm{s}^2$, $W = (-2.22+0.013)\times10^{-15}\,\mathrm{cm}^{-1}\,\mathrm{s}^2$. The characteristic absorption length $L_A = 1/|\alpha| = 73\,\mathrm{cm}$. The results show that the real parts of K_2 and W are much greater than the imaginary parts, and that L_A is also an order of magnitude greater than L_D, so we can ignore absorption of the probe light by the surface-polarization exciton during the formation process. Similarly, for antisymmetric SPPs, we use $\Gamma_{31} = 0.017\,\Gamma$, $\Delta_2 = 2.33\,\Gamma$, $\Delta_3 = -0.04\,\Gamma$, and $\tau_0 = 6\times10^{-6}\,\mathrm{s}$, and we calculate $\mathrm{Im}(K+k) = 0.0037\,\mathrm{cm}^{-1}$. In addition, we get $L_D = 0.3\,\mathrm{cm}$, $K_2 = (1.04+0.18)\times10^{-10}\,\mathrm{cm}^{-1}\,\mathrm{s}^2$, $W = (-1.15-0.00021)\times10^{-15}\,\mathrm{cm}^{-1}\,\mathrm{s}^2$. The characteristic absorption length $L_A = 1/|\alpha| = 274\,\mathrm{cm}$. As with the symmetric mode, $L_A \gg L_D$ for the antisymmetric mode, so absorption of the probe light by the system is negligible. In addition, by selecting a suitable incoherent pumping, both the symmetric and antisymmetric mode can form SPPs solitons capable of stable propagation in the MDM waveguide.

We numerically simulate the propagation of SPPs solitons and analyze their stability by using MB equations (5) and (6). Figure 6 shows a schematic diagram of electric field intensity distribution of $|\mathbf{E}_p(x,z,t)|$ and wave shape of $|\Omega_p(z,t)/U_0|$ during propagation of antisymmetric and symmetric SPPs. Note that we together show the spatial profile of the electric field in seven different moments, thus the seven peaks in z direction is not the field oscillations but the field in seven different moment. The initial condition for the numerical solution is $\Omega_p(0,t) = U_0 sech(t/\tau_0)$ (thus $\mathbf{E}_p(x,0,t) = (\hbar U_0/|\mathbf{p}_{12}|)\times\mathbf{u}_\mathbf{p}(x)sech(t/\tau_0)$). When plotting $|\mathbf{E}_p|$, we have normalized the initial peak value of $|\mathbf{E}_p|$ to 1. Figure 6a shows a schematic diagram of the intensity distribution $|\mathbf{E}_p|$ of antisymmetric-mode SPPs for a relatively weak nonlinearity. As shown in the figure, with propagation distance increasing, the intensity of the SPPs in the antisymmetric mode weakens and the width of the distributed region of SPPs widens, which reflects a clear dispersion of SPPs that cannot be balanced by the

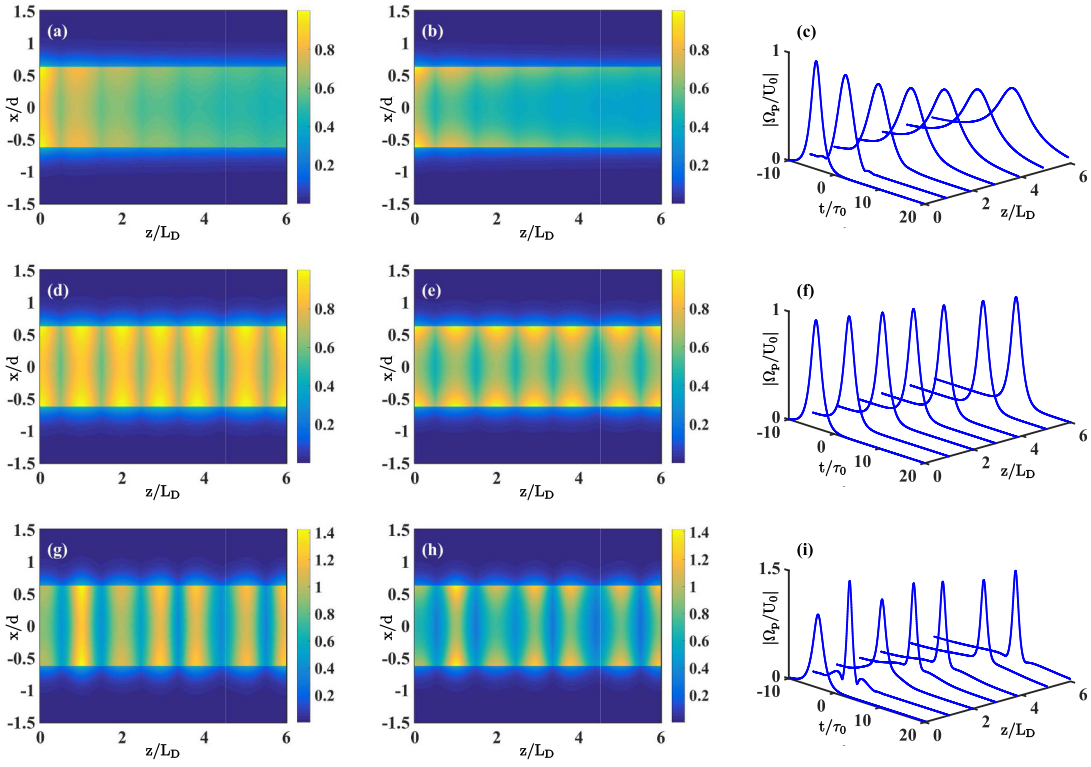

Fig. 6. The time dynamic of electric field intensity distribution of $|\mathbf{E}_p|$ and wave shape of $|\Omega_p/U_0|$ during propagation of antisymmetric and symmetric SPPs: (a), (d), (g) are electric field intensity distribution $|\mathbf{E}_p|$ of SPPs in antisymmetric mode as a function of z/L_D and x/d. (b), (e), (h) are electric field intensity distribution $|\mathbf{E}_p|$ of SPPs in symmetric mode as a function of z/L_D and x/d. (c), (f), (i) are wave shape of $|\Omega_p/U_0|$ as a function of z/L_D and t/τ_0. Different rows correspond to different nonlinearity levels (from top to the end correspond for weak, medium and strong nonlinearity respectively). Note that we together show the spatial profile of the electric field in seven different moments, thus the seven peaks in z direction are not the field oscillations but the field in seven different moments.

nonlinearity, so that the SPPs cannot maintain its shape during propagation.

Figure 6b shows a schematic diagram of the intensity distribution $|\mathbf{E}_p|$ of symmetric-mode SPPs for relatively weak nonlinearity. Similar to the case of the antisymmetric mode, SPPs cannot maintain their shape as they propagate in symmetric mode. Figure 6c shows a more clear physical picture of this effect for both antisymmetric-mode and symmetric-mode SPPs. With weak nonlinearity, as the propagation distance increasing, the pulse broaden seriously in time dimension, thus the intensity of the SPPs weakens.

Figure 6d shows, for moderate nonlinearity, the propagation of antisymmetric-mode SPPs. We find a set of suitable system parameters for which, with increasing propagation distance, the strength of the antisymmetric-mode SPPs remains basically constant, as does the SPPs distribution width. This result is attributed to the nonlinearity just balancing the dispersion, so that a stable propagating SPPs soliton is formed. We also find a set of suitable parameters to balance the dispersion and the nonlinearity, thereby forming the symmetric-mode SPPs soliton shown in Figure 6e. In the moderate nonlinearity case, the pulse width keeps almost the same during the propagation of SPPs as illustrated in Figure 6f. Figure 6g shows the situation when the nonlinearity is too strong for the propagation of antisymmetric-mode SPPs. This result shows that, with increasing propagation distance, the intensity of the SPPs becomes stronger first and then weakens, and the width of the SPPs distribution region first narrows and then broadens. Therefore, SPPs solitons cannot form when the nonlinearity is too strong. The same result is obtained for symmetric-mode SPPs, as shown in Figure 6h. Due to the strong nonlinearity, the wave shape $|\Omega_p/U_0|$ can not maintain and changes a lot, as shown in Figure 6i.

5 Summary

In this work, we study in detail the propagation of symmetric and antisymmetric SPPs solitons generated in an MDM waveguide structure interacting with a ladder-type EIT system. In the linear propagation regime, we first study the relationship between incoherent pumping rate Γ_{31} and the active gain $-\mathrm{Im}(K)$ and find that the gain for both modes increases with increasing Γ_{31}, and that the gain does not increase once the absorption saturates for antisymmetric mode. By calculating the group velocity, we find that both modes can propagate as slow light.

In the nonlinear propagation regime, the results indicate that the Kerr nonlinearity can be strongly enhanced by the symmetric and antisymmetric SPPs, although the different modes are generated by different incoherent pumping intensities. Finally, the numerical simulation indicates that gain-assisted (1+1)-dimensional symmetric and antisymmetric subluminal SPPs solitons may be produced by exploiting the strong confinement of the electric field in the MDM waveguide. These results should help guide future studies of SPPs soliton propagation[3].

This work was supported by National Natural Science Foundation of China (NSFC) under grants No. 11604185 and No. 11804196 and by the China Postdoctoral Science Foundation under grant No. 2017M612323.

Author contribution statement

Zhenning Gu performed the derivation and most of numerical calculations, and drafted the manuscript. Qi Liu helped for some numerical calculations. Chaohua Tan conceived the idea and analyzed the results. All authors participated in the discussion and review of the results, and contributed to the revision of the manuscript.

Appendix A: The TM electromagnetic field mode in MDM waveguide

In this article we consider only the TM polarized mode of electromagnetic(EM) field. The coordinate system is set as illusted in Figure 1a. From Maxwell equations without charge and current source, we obtain

$$\left(\nabla^2 - \frac{\varepsilon_r \mu_r}{c^2}\frac{\partial^2}{\partial t^2}\right)\mathbf{H} = 0, \tag{A.1a}$$

$$\frac{\partial}{\partial t}\mathbf{E} = \frac{1}{\varepsilon_0 \varepsilon_r}\nabla \times \mathbf{H}, \tag{A.1b}$$

where $\mathbf{E}$ and $\mathbf{H}$ are electric field and magnetic field, c is the speed of light in vacuum, μ_r is relative permeability, ε_r is relative permittivity, ε_0 is permittivity in vacuum. We assume the EM field propagetes in the positive z with harmonic frequency ω_l, for TM polarized mode, $\mathbf{E}$ and $\mathbf{H}$ can be written as

$$\mathbf{H} = \mathbf{e}_y H_y(x) e^{i(kz-\omega_l t)}, \tag{A.2a}$$

$$\mathbf{E} = \left(\mathbf{e}_x E_x(x) + \mathbf{e}_z E_z(x)\right) e^{i(kz-\omega_l t)}. \tag{A.2b}$$

[3] Such approach is similar to the averaging method used in references [36,37]. A more rigorous approach should account for nonlinear terms in boundary conditions and nontransverse character of the electric field. In this way, the mode function in high-order approximations will be a little different. However, as shown by Marini and Skryabin [49], the difference between the two approaches is not significant if the wavelength of the excitation is not too short.

Here $\mathbf{e}_\alpha(\alpha = x, y, z)$ is unit vector of α axis, k is propagation constant. Then equation (A.1) reads

$$\frac{d}{dx}H_y(x) - k_{xl}^2 H_y(x) = 0, \tag{A.3a}$$

$$E_x(x) = \frac{k}{\varepsilon_r \omega_l}H_y(x), E_z(x) = -\frac{i}{\varepsilon_r \omega_l}H_y(x), \tag{A.3b}$$

with $k_{xl}^2 = k^2 - \varepsilon_l \mu_l k_0^2$ ($l = 1$ for dielectric, $l = 2$ for metal). We divide the space into three region according to x coordinate:region one, $x > d/2$; region two, $|x| < d/2$; region three, $x \leq -d/2$. The physical picture of DMD waveguide is that the $\mathbf{H}$ field will mainly confined in region two (dieletric layer), thus $\mathbf{H}$ will exponential decay beyond region two. Then the physical solution of equation (A.3a) is

$$H_y(x) = \begin{cases} A \cdot \cosh(k_{xl}x + \psi), & |x| < \frac{d}{2} \\ B \cdot e^{-k_{xl}x}, & x \geq \frac{d}{2} \\ C \cdot e^{k_{xl}x}, & x \leq -\frac{d}{2} \end{cases} \tag{A.4}$$

with A, B, C are constant to be determined, $\psi = mi\pi/2$ ($m = 0$ for symmetric mode, $m = 1$ for antisymmetric mode). Then $\mathbf{E}$ can be determined via equation (A.3b). The boundary conditions alone two metal-dielectric interface reads $\mathbf{e}_x \times (\mathbf{H}_2 - \mathbf{H}_1) = 0, \mathbf{e}_x \times (\mathbf{E}_2 - \mathbf{E}_1) = 0$, which means $H_y(x)$ and $E_z(x)$ should be continuous at $x = \pm d/2$. The boundary conditions yield

$$A \cdot \cosh\left(\frac{dk_{x1}}{2} + \psi\right) = B \cdot e^{-\frac{d}{2}k_{x2}}, \tag{A.5a}$$

$$A \cdot \cosh\left(\frac{dk_{x1}}{2} - \psi\right) = C \cdot e^{-\frac{d}{2}k_{x2}}, \tag{A.5b}$$

$$-\frac{iA \cdot k_{x1}\sinh\left(\frac{dk_{x1}}{2} + \psi\right)}{\omega_l \varepsilon_d} = \frac{iB \cdot k_{x2} e^{-\frac{d}{2}k_{x2}}}{\omega \varepsilon_2}, \tag{A.5c}$$

$$\frac{iA \cdot k_{x1}\sinh\left(\frac{dk_{x1}}{2} - \psi\right)}{\omega_l \varepsilon_1} = -\frac{iC \cdot k_{x2} e^{-\frac{d}{2}k_{x2}}}{\omega \varepsilon_2}, \tag{A.5d}$$

thus we get $B = A \cdot \cosh(dk_{x1}/2 + \psi) \cdot \exp(dk_{x2}/2)$, $C = A \cdot \cosh(dk_{x1}/2 - \psi) \cdot \exp(dk_{x2}/2)$. Then from equation (A.5c) or (A.5d), we obtain the dispersion relation

$$\frac{k_{x2}}{\varepsilon_2} + \frac{k_{x1}}{\varepsilon_1}\tanh\left(\frac{d \cdot k_{x1}}{2} + \psi\right) = 0. \tag{A.6}$$

Now we can write down the mode field

$$\mathbf{E} = \begin{cases} \frac{A}{\omega\varepsilon_1}\left[\mathbf{e}_x k\cosh(k_{x1}x + \psi) - i\mathbf{e}_z k_{x1}\sinh(k_{x1}x + \psi)\right] \\ \quad e^{i(kz-\omega_l t)}, |x| < \frac{d}{2} \\ \frac{A}{\omega\varepsilon_2}\left(\mathbf{e}_x k + i\mathbf{e}_z k_{x2}\right) \\ \quad \cdot\cosh\left(\frac{dk_{x1}}{2} + \psi\right) \cdot e^{-k_{x2}(x-\frac{d}{2})} e^{i(kz-\omega_l t)}, x \geq \frac{d}{2} \\ \frac{A}{\omega\varepsilon_2}\left(\mathbf{e}_x k - i\mathbf{e}_z k_{x2}\right) \\ \quad \cdot\cosh\left(\frac{dk_{x1}}{2} - \psi\right) \cdot e^{k_{x2}(x+\frac{d}{2})} e^{i(kz-\omega_l t)}, x \leq -\frac{d}{2} \end{cases} \tag{A.7a}$$

$$\mathbf{H} = \begin{cases} A \cdot \cosh(k_{x1}x + \psi) e^{i(kz-\omega_l t)}, |x| < \frac{d}{2} \\ A \cdot \cosh\left(\frac{dk_{x1}}{2} + \psi\right) \cdot e^{-k_{x2}(x-\frac{d}{2})} e^{i(kz-\omega_l t)}, x \geq \frac{d}{2} \\ A \cdot \cosh\left(\frac{dk_{x1}}{2} - \psi\right) \cdot e^{k_{x2}(x+\frac{d}{2})} e^{i(kz-\omega_l t)}, x \leq -\frac{d}{2}. \end{cases} \tag{A.7b}$$

Appendix B: Second order solutions of equations $\sigma_{ij}^{(2)}$

$$\sigma_{11}^{(2)} = \frac{[-i\Gamma_{23} + 2|\zeta_c(x)\Omega_c e^{i\theta_c}|^2(\frac{1}{d_{32}} - \frac{1}{d_{32}^*})](\frac{D_1^*}{D^*} - \frac{D_1}{D}) + i\Gamma_{12}\Omega_c(\frac{\zeta_c^*(x)e^{-i\theta_c^*}}{d_{32}}\frac{D_2}{D} - \frac{\zeta_c(x)e^{-i\theta_c}}{d_{32}^*}\frac{D_2^*}{D^*})}{(\Gamma_{23}\Gamma_{12} + \Gamma_{23}\Gamma_{31} + \Gamma_{31}\Gamma_{12}) + i(\Gamma_{12} + 2\Gamma_{31})|\zeta_c(x)\Omega_c e^{i\theta_c}|^2(\frac{1}{d_{32}} - \frac{1}{d_{32}^*})}$$
$$\times |\zeta_p(x)e^{i\theta_p}|^2|F|^2e^{-2\bar{\alpha}z_2}$$
$$= a_{11}^{(2)}|\zeta_p(x)e^{i\theta_p}|^2|F|^2e^{-2\bar{\alpha}z_2},$$
$$\sigma_{22}^{(2)} = \frac{\Gamma_{31}a_{11}^{(2)} + i(\frac{D_1^*}{D^*} - \frac{D_1}{D})}{\Gamma_{12}} \times |\zeta_p(x)e^{i\theta_p}|^2|F|^2e^{-2\bar{\alpha}z_2}$$
$$= a_{22}^{(2)}|\zeta_p(x)e^{i\theta_p}|^2|F|^2e^{-2\bar{\alpha}z_2},$$
$$\sigma_{32}^{(2)} = \frac{[\frac{D_2}{D} - \zeta_c(x)\Omega_c(2a_{22}^{(2)} + a_{11}^{(2)})]}{d_{32}} \times |\zeta_p(x)e^{i\theta_p}|^2|F|^2e^{-2\bar{\alpha}z_2}$$
$$= a_{32}^{(2)}|\zeta_p(x)e^{i\theta_p}|^2|F|^2e^{-2\bar{\alpha}z_2},$$
$$\sigma_{21}^{(2)} = i\frac{D_2\zeta_c^*(x)\Omega_c^*e^{-i\theta_c^*} - D_1(\omega + d_{31})}{D^2}\zeta_p(x)\frac{\partial F}{\partial t_1}e^{i\theta}e^{i\theta p}$$
$$= a_{21}^{(2)}\zeta_p(x)\frac{\partial F}{\partial t_1}e^{i\theta}e^{i\theta p},$$
$$\sigma_{31}^{(2)} = -\frac{1}{\zeta_c^*(x)\Omega_c^*(z)e^{-i\theta_c^*}}[i\frac{D_1}{D} + (\omega + d_{21})a_{21}^{(2)}]\zeta_p(x)\frac{\partial F}{\partial t_1}e^{i\theta}e^{i\theta_p}$$
$$= a_{31}^{(2)}\zeta_p(x)\frac{\partial F}{\partial t_1}e^{i\theta}e^{i\theta_p},$$

where $\bar{\alpha} = \epsilon^{-2}\mathrm{Im}[\mathrm{K}(\omega)], \theta = K(\omega)x_0 - \omega t_0$.

References

1. H. Ditlbacher, J.R. Krenn, G. Schider, A. Leitner, F.R. Aussenegg, Appl. Phys. Lett. **81**, 1762 (2002)
2. S.I. Bozhevolnyi, V.S. Volkov, E. Devaux, J.-Y. Laluet, T.W. Ebbesen, Nature **440**, 508 (2006)
3. P. Li, Y. Wang, P. Xu, Appl. Optics **58**, 4205 (2019)
4. T. Sun, H. Chen, S. Yang, J. Hu, C. Wang, Opt. Laser Technol. **108**, 551 (2018)
5. P. Manley, F.F. Abdi, S. Berglund, A.N. Islam, S. Burger, R. van de Krol, M. Schmid, ACS Appl. Energy Mater. **1**, 5810 (2018)
6. W. Ahn, I. Vurgaftman, J.J. Pietron, P.E. Pehrsson, B.S. Simpkins, J. Mater. Chem. A **7**, 7015 (2019)
7. B. Ruan, Q. You, J. Zhu, L. Wu, J. Guo, X. Dai, Y. Xiang, Sensors **18**, 2098 (2018)
8. J. Kenison, Nonlinear microscopy with surface plasmon polaritons, Ph.D. thesis, UC Irvine, 2018
9. J.M. Jornet, I.F. Akyildiz, IEEE J. Sel. Areas Commun. **31**, 685 (2013)
10. X. Guo, J. Du, Y. Guo, J. Yao, Opt. Lett. **31**, 2613 (2006)
11. A. Kamli, S.A. Moiseev, B.C. Sanders, Phys. Rev. Lett. **101**, 263601 (2008)
12. S. Asgarnezhad-Zorgabad, R. Sadighi-Bonabi, B.C. Sanders, Phys. Rev. A **98**, 013825 (2018)
13. B.R. Lavoie, P.M. Leung, B.C. Sanders, Phys. Rev. A **88**, 023860 (2013)
14. C. Tan, G. Huang, Phys. Rev. A **89**, 033860 (2014)
15. L. Deng, M.G. Payne, Phys. Rev. Lett. **98**, 253902 (2007)
16. K.J. Jiang, L. Deng, M.G. Payne, Phys. Rev. A **74**, 041803 (2006)
17. A.S. Zibrov, M.D. Lukin, D.E. Nikonov, L. Hollberg, M.O. Scully, V.L. Velichansky, H.G. Robinson, Phys. Rev. Lett. **75**, 1499 (1995)
18. H. Schempp, G. Günter, C.S. Hofmann, C. Giese, S.D. Saliba, B.D. DePaola, T. Amthor, M. Weidemüller, S. Sevinçli, T. Pohl, Phys. Rev. Lett. **104**, 173602 (2010)
19. S. Asgarnezhad-Zorgabad, P. Berini, B.C. Sanders, Phys. Rev. A **99**, 051802 (2019)
20. F. Abdullaev, S. Darmanyan, P. Khabibullaev, J. Engelbrecht, *Optical Solitons* (Springer Publishing Company, Incorporated, 2014)
21. J. Su, D. Xu, G. Huang, ACS Photonics **5**, 2496 (2018)
22. H. Kubota, M. Nakazawa, Opt. Commun. **87**, 15 (1992)
23. B. Wang, G.P. Wang, Opt. Lett. **29**, 1992 (2004)
24. S. Aldawsari, L. Wei, W.-K. Liu, J. Lightwave Technol. **33**, 3198 (2015)
25. Z. He, H. Li, B. Li, Z. Chen, H. Xu, M. Zheng, Opt. Lett. **41**, 5206 (2016)
26. Y. Huang, C. Min, G. Veronis, Opt. Express **20**, 22233 (2012)
27. D.-W. Kim, J.-H. Lee, Microw. Opt. Technol. Lett. **43**, 426 (2004)
28. M. Ando, J. Hirokawa, T. Yamamoto, A. Akiyama, Y. Kimura, N. Goto, IEEE Trans. Microw. Theory Tech. **46**, 792 (1998)
29. G. Veronis, S. Fan, J. Lightwave Technol. **25**, 2511 (2007)
30. A. Bhaumik, D. Ghoshal, Hybrid dielectric-loaded surface plasmonic waveguide, in *International Conference on Communication and Signal Processing (ICCSP)* (IEEE, 2016), p. 1579
31. J. Chen, Z. Li, S. Yue, Q. Gong, Opt. Express **17**, 23603 (2009)

32. H. Lu, X. Liu, D. Mao, G. Wang, Opt. Lett. **37**, 3780 (2012)
33. A.D. Boardman, G.S. Cooper. Phys. Rev. B **34**, 8273 (1986)
34. W. Walasik, V. Nazabal, M. Chauvet, Y. Kartashov, G. Renversez, Opt. Lett. **37**, 4579 (2012)
35. W. Walasik, G. Renversez, Y.V. Kartashov, Phys. Rev. A **89**, 023816 (2014)
36. E. Feigenbaum, M. Orenstein, Opt. Lett. **32**, 674 (2007)
37. A.R. Davoyan, I.V. Shadrivov, Y.S. Kivshar, Opt. Express **17**, 21732 (2009)
38. K.Y. Bliokh, Y.P. Bliokh, A. Ferrando, Phys. Rev. A **79**, 041803(R) (2009)
39. D.K. Gramotnev, S.I. Bozhevolnyi, Nat. Photonics **4**, 83 (2010)
40. G. Veronis, Z. Yu, S.E. Kocabas, D.A. Miller, M.L. Brongersma, S. Fan, Chin. Opt. Lett. **7**, 302 (2009)
41. C. Tan, G. Huang, Phys. Rev. A **91**, 023803 (2015)
42. T. Naseri, S.H. Asadpour, R. Sadighi-Bonabi, J. Opt. Soc. Am. B **30**, 641 (2013)
43. R. Wan, F. Liu, X. Tang, Y. Huang, J. Peng, Appl. Phys. Lett. **94**, 141104 (2009)
44. Z. Han, S.I. Bozhevolnyi, Rep. Prog. Phys. **76**, 016402 (2012)
45. J.A. Dionne, E. Verhagen, A. Polman, H.A. Atwater, Opt. Express **16**, 19001 (2008)
46. C. Tan, G. Huang, Phys. Rev. A **89**, 033860 (2014)
47. Q. Liu, C. Tan, Eur. Phys. J. D **72**, 99 (2018)
48. G. Huang, K. Jiang, M. Payne, L. Deng, Phys. Rev. E **73**, 056606 (2006)
49. A. Marini, D.V. Skryabin, Phys. Rev. A **81**, 033850 (2010)
50. C. Shou, G. Huang, Phys. Rev. A **100**, 063844 (2019)
51. J. Su, D. Xu, G. Huang, ACS Photonics **5**, 2496 (2018)